Wang, Zulin; Yliniemi, Kirsi; Wilson, Benjamin P.; Lundström, Mari

# Targeted surface modification of Cu/Zn/Ag coatings and Ag/Cu particles based on sacrificial element selection by electrodeposition and redox replacement

*Published in:*
Surface and Coatings Technology

*DOI:*
10.1016/j.surfcoat.2022.128531

Published: 15/07/2022

*Document Version*
Publisher's PDF, also known as Version of record

Surface & Coatings Technology 441 (2022) 128531

Contents lists available at ScienceDirect

Surface & Coatings Technology

journal homepage: www.elsevier.com/locate/surfcoat

# Targeted surface modification of Cu/Zn/Ag coatings and Ag/Cu particles based on sacrificial element selection by electrodeposition and redox replacement

Zulin Wang [a], Kirsi Yliniemi [b], Benjamin P. Wilson [a], Mari Lundström [a,*]

[a] Department of Chemical and Metallurgical Engineering (CMET), School of Chemical Engineering, Aalto University, P.O. Box 16200, Vuorimiehentie 2, 02150 Espoo, Finland

[b] Department of Chemistry and Materials Science (CMAT), School of Chemical Engineering, Aalto University, P.O. Box 16100, Kemistintie 1, 02150 Espoo, Finland

ARTICLE INFO

*Keywords:*
Metals circular economy
Materials design
Cyanide-free electroplating
Corrosion resistance
Optical properties

ABSTRACT

The electrodeposition-redox replacement (EDRR) method was investigated for the preparation of two types of functional surfaces. A synthetic solution simulating Zn process solution containing 65 g/L Zn, 200 ppm Cu, 2 ppm Ag and 10 g/L $H_2SO_4$ was used as the source for creating functional surfaces EDRR experiments. The effects of operating parameters such as deposition potential ($E_1$), deposition time ($t_1$), and redox replacement time ($t_2$) have been comprehensively studied. When $E_1$ was selected to deposit Zn as the sacrificial metal, coherent Cu/Zn/Ag coatings with various chemical compositions, crystalline phases and surface morphology were obtained depending on the selected $t_1$ and $t_2$. The Cu/Zn/Ag coatings also exhibited competitive corrosion resistance ($E_{corr}$ = −683 to −634 mV vs. $Hg/Hg_2SO_4$, $j_{corr}$ = 1.6–4.1 μA/cm$^2$) when compared to those detailed in the literature. In contrast, when $E_1$ was selected so that Cu was the sacrificial metal, separated Cu/Ag particles with controllable chemical composition, particle size (82–170 nm) and tunable surface plasmon resonance (SPR) behavior were formed through the variation of $t_1$ and $t_2$. In addition to the ability to tailor different functionalities for the surfaces from the same solutions, the process was performed in a single electrochemical cell without the addition of any complexing agents. Overall, these promising results demonstrated the versatility of the EDRR method to create various high value-added functional materials from complex hydrometallurgical solutions which contain multiple metal impurities.

## 1. Introduction

Functional materials with special physical, chemical or biological properties are of great importance in modern society due to their applicability in upgrading traditional industries and boosting the advancement of high-tech fields like biotechnology and energy technology [1]. Cu/Zn-based (known as brass) coatings are a type of metallic functional materials that have attracted great attention due to their wide applications like corrosion prevention, decoration, electronics, catalysts, and energy storage [2–5]. Silver-based nanoscale particle decorated surfaces, on the other hand, represent another category of functional surfaces that are currently the subject of intensive research due to their outstanding conductive, optical, catalytic and antimicrobial properties [6–9]. Recently, Ag bimetallic nanoparticles with surface plasmonic resonance have attracted attention due to the possibility of obtaining multi-functionality/enhanced properties by selecting appropriate metal combinations [10].

Electrodeposition has been one of the most common methods for the preparation of brass coatings and silver-based nanoparticles from aqueous solutions due to the advantages of low costs, convenience and tunable product properties that can be precisely controlled via operating parameters. However, traditional electrodeposition has also some drawbacks when considering sustainability: for instance, complexing agents are needed during brass electrodeposition due to the significant difference between the standard reduction potentials of $Cu^{2+}$/Cu and $Zn^{2+}$/Zn redox pairs. Toxic cyanide has been the most widely used complexing agent for brass electroplating [2,11] although a variety of other chemicals like pyrophosphate [12], citrate [13], EDTA [14], glutamate [15], sorbitol [16], glycine [17], etc. have been investigated. Recently, non-aqueous electrolytes like ionic liquids and deep eutectic

* Corresponding author.
*E-mail address:* mari.lundstrom@aalto.fi (M. Lundström).

https://doi.org/10.1016/j.surfcoat.2022.128531
Received 2 February 2022; Received in revised form 18 April 2022; Accepted 8 May 2022
Available online 16 May 2022

solvents have also attracted great attention for brass electrodeposition due to their wide electrochemical windows, vapor pressure, and high ionic conductivity [18–20] - however, the commercial application of these baths has so far been limited by the high prices. On the other hand, the demand for Zn, Cu and Ag has been ever-increasing with the advancement of the industrial world and a growing global population, while high-grade raw materials are depleting [21–23]. Consequently, the search for new and environmentally-friendly practices and alternative raw materials for the production of brass coatings and Ag-based materials has become increasingly important for the realization of sustainable concepts.

During the hydrometallurgical production of base metals like Cu, Zn, Ni and Pb, precious metals (Ag, Pt, Au, etc.) are also present in process solutions, due to their coexistence within the ore bodies [24–29]. Consequently, such solutions could function as attractive raw materials sources for the direct production of high-value material surfaces. Nonetheless, the precious metals present in these types of hydrometallurgical solutions are present at only minor concentrations (ppm level or even lower) and therefore underutilized. Recently, the innovation of electrodeposition-redox replacement (EDRR) has enabled the recovery of trace amounts of Ag, Pt, Au and Te (ppm level or lower) from hydrometallurgical base metal solutions [30–37]. Lately, studies have demonstrated the possibility to produce value-added functional Pt/Ni, Cu/Ag and Ag/Zn particles using the EDRR method [38–40]. However, these studies were mainly conducted in two-metal solutions, while in practice hydrometallurgical process solutions typically have more complex compositions. For instance, in addition to Ag, Cu is a typical impurity present in Zn process solutions and requires an additional solution purification step to avoid Cu contamination of the final products [41–44]. On the other hand, the presence of Cu offers variance for EDRR operation with solutions containing $Zn^{2+}$/Zn and $Ag^{+}$/Ag pairs. The versatility of EDRR allows for different surface modifications to be targeted – and hence applications – from the same solution, by choosing appropriate related parameters to select either Zn or Cu as the desired sacrificial metal. The direct preparation of brass coatings using EDRR is extremely attractive due to the possibility to combine metals with distinct potentials without any complexing agents when compared with traditional electrodeposition. On the other hand, the combination of Ag with base metals like Cu is also interesting, not only due to the possible new bifunctional or synergistic effects but also because of the minimized usage of expensive and dwindling precious Ag. Although the EDRR between Cu and Ag has been investigated previously, the research only revealed the effects of the mass-transfer limitations of the noble metal (Ag) within comparatively concentrated Cu-solutions (40 g/L Cu) [38]. However, the mass-transfer effects of the sacrificial metals with significantly lower Cu levels (hundreds of ppm) in Zn process solutions have not been investigated. Also, the crystalline-phase compositions of whether Cu and Ag exist as independent phases within individual particles have yet to be further characterized. Moreover, the potential application of the Cu/Ag particles formed by EDRR needs to be further explored in detail.

This study aims at using the EDRR method to directly create functional surfaces via a single-cell configuration from a simulated hydrometallurgical process solution containing Zn at high concentration (g/L) and ppm-levels of Cu and Ag by the selection of either Zn or Cu as the sacrificial metal. Two types of materials are targeted; (i) coherent Cu/Zn/Ag coatings obtained using Zn as the sacrificial metal, and (ii) separated Cu/Ag nanoparticles using Cu as sacrificial metal. Moreover, the potential applications of the deposits as anti-corrosive materials or with plasmon resonance behavior are investigated.

## 2. Material and methods

The electrochemical experiments were carried out in a three-electrode cell (50 $cm^3$) at room temperature (21 ± 0.5 °C). A potentiostat (IviumStat 24-bit CompactStat, Ivium Technologies, The Netherlands) was used to control and monitor all the electrochemical experiments. A platinum plate (exposed area of 9 $cm^2$) was used as the counter electrode (CE), glassy carbon plates (the side facing the counter electrode was exposed, area of 1.0 $cm^2$) functioned as the working electrode (WE) and the reference electrode (RE) was a mercury/mercurous sulfate electrode ($Hg/Hg_2SO_4$, filled with saturated $K_2SO_4$ solution, +0.650 *V* vs. a standard hydrogen electrode (SHE)). The distance between the WE and CE was kept fixed at 2 cm. Prior to the electrochemical measurements, working electrodes were cleaned by sonication in ethanol, and this was followed by rinsing with DI water before application of an electrochemical cleaning process that comprised 10 cycles of cyclic voltammetry (C*V*) in a 0.1 M $H_2SO_4$ solution between −1.0 V and + 1.2 V (vs. $Hg/Hg_2SO_4$) with a scan rate of 50 mV/s. Once electrochemically cleaned samples were thoroughly rinsed with DI water and finally dried in air. A simulated zinc process solution (pH = 1.2) containing 65 g/L Zn (from $ZnSO_4$, ≥99 wt%, VWR chemicals, Belgium), 200 ppm Cu (from $CuSO_4{\cdot}5H_2O$, ≥98 wt%, Sigma Aldrich, U.S.A.), 2 ppm Ag (from $AgNO_3$, ≥99.0 wt%, Sigma-Aldrich, U.S.A.) and 10 g/L $H_2SO_4$ ($H_2SO_4$, 95–97%, EMD Millipore, Germany) was used as the electrolyte for the electrodeposition-redox replacement (EDRR) method. All the solutions were prepared with Millipore Milli-Q deionized water (DI water, resistance ≥18 MΩ·cm).

Zn/Cu/Ag coating and Cu/Ag particles were prepared on the GC electrodes using 200 repetitive EDRR cycles – in both cases the same solution composition was used, i.e. the only difference was in the EDRR parameters selected. A single EDRR cycle consists of two steps: Firstly, a sacrificial metal with a relatively negative redox potential is deposited at potential $E_1$ for a short time duration, $t_1$ (ED step). In the second step, the applied external potential is switched off and the working electrode is left at open circuit potential (OCP) for a time duration of $t_2$, during which redox replacement reactions spontaneously commence between the less noble metal (also called as a sacrificial metal) deposited on the electrode and more noble metal ions present in the solution (RR step): no external potential or current is applied during the RR step, but there is an associated change in open circuit potential which is merely recorded during this step.

The appropriate $E_1$ values in ED step were selected either for Zn or Cu deposition, as determined from a series of cyclic voltammetric studies (potential range of −1.6 to +0.5 *V* and − 1.0 to +0.5 V (vs. $Hg/Hg_2SO_4$)) with a scan rate of 20 m*V*/s in the solutions used for EDRR experiments (65 g/L Zn, 200 ppm Cu, 2 ppm Ag and 10 g/L $H_2SO_4$). Zn/Cu/Ag coatings were prepared using Zn as the sacrificial metal with an $E_1$ of −1.55 *V* (vs. $Hg/Hg_2SO_4$), $t_1$ of 0.3–0.5 s and $t_2$ of 5–20 s. In contrast, Cu/Ag particles were produced using Cu as the sacrificial metal with an $E_1$ of −0.70 V (vs. $Hg/Hg_2SO_4$), $t_1$ of 0.3–0.5 s and $t_2$ of 2–10 s. All the EDRR experiments were conducted under 100-rpm magnetic stirring to improve the mass-transfer conditions. Following the EDRR experiments, the working electrodes were immediately removed from the solution, cleaned with DI water, and dried in air.

The microstructure and the chemical composition of the EDRR products were characterized by a Mira$^2$ Tescan GM (Czech Republic) scanning electron microscope equipped with energy-dispersive X-ray spectroscopy (EDS, Thermo Fisher Scientific, U.S.A.). The reported chemical compositions (as atom percent) of the deposits were average EDS values of 10 point/area spectra measured at randomly selected points on the samples (N.B. the background carbon signals were excluded). The particle size (diameter) of Cu/Ag particles was analyzed from SEM micrographs using ImageJ software based on the average diameter of at least 100 particles per sample. Anodic linear sweep voltammetry (ALS*V*) was performed for the EDRR products in a 0.1 M $H_2SO_4$ between the potential window of −1.0 V to +1.0 V (vs. $Hg/Hg_2SO_4$) at a scan rate of 5 mV/s. The stripping charge density ($Q_s$) of the anodic peak was calculated based on the integration of current density as a function of time as shown in Eq. (1):

$$Q_s = \int_{t_a}^{t_b} j(t)\mathrm{d}t \quad (1)$$

where $t_a$ and $t_b$ are the starting and the ending time points of the anodic peak(s) as presented in supplementary material (Fig. S1), $j$ is the current density (mA/cm$^2$) and $Q_s$ is the stripping charge density (mC/cm$^2$).

The cathodic charge density during the ED steps of 200 EDRR cycles was calculated based on Eq. (2):

$$Q_c = |\Sigma_{k=1}^{200}(i_k \times t_k)| \quad (2)$$

where $i_k$ (mA/cm$^2$) is the average current density in the ED step of $k^{\text{th}}$ EDRR cycle, $t_k$ (s) is time duration of the ED step of $k^{th}$ EDRR cycle and $Q_c$ is the absolute value of cathodic charge density of during the ED steps 200 EDRR cycles.

The overall current efficiency ($\eta$) was calculated based on the stripping charge density ($Q_s$) and The cathodic charge density ($Q_c$) using Eq. (3):

$$\eta = (Q_s/Q_c) \times 100\% \quad (3)$$

Crystalline phases of the samples were identified by X-ray diffraction (XRD, Cu Kα radiation source, PANalytical X'Pert ProPowder, Almelo, The Netherlands) at a scan speed of 0.1°/min over a 2θ (°) range between 10° and 90° (acceleration potential 40 kV and current 40 mA) and HighScore 4.0 Plus software was used for the analysis of the XRD patterns.

Corrosion performance of the deposited Cu/Zn/Ag coatings was evaluated by potentiodynamic polarization measurements using the same electrochemical cell as the EDRR experiments in a 3.5 wt% NaCl solution (from NaCl, ≥ 98 wt%, Sigma-Aldrich, U.S.A.) at room temperature. Prior to the corrosion tests, samples were immersed in the NaCl solution for 30 min to achieve a stable open circuit potential. Potentiodynamic scans were performed between −300 mV and + 250 mV (vs. OCP) at a sweeping speed of 0.5 mV/s. The Tafel extrapolation method was used to estimate the values of corrosion potential ($E_{corr}$) and corrosion current density ($j_{corr}$) from polarization curves.

In addition, the optical properties of the Cu/Ag particles were characterized by ultraviolet-visible diffuse reflectance spectroscopy (UV/VIS, Shimadzu UV-2600 UV/VIS spectrometer, Japan). The absorbance spectra (A) were calculated based on the reflectance spectra (R) via Eq. (4):

$$A = 100\% - R \quad (4)$$

where A is the absorbance (%) and R is the reflectance (%).

## 3. Results and discussion

### 3.1. Determination of deposition potential $E_1$

In this study, three redox pairs related to the metal elements ($Zn^{2+}$/Zn, $Cu^{2+}$/Cu and $Ag^{+}$/Ag) are involved in the electrodeposition-redox replacement processes. The driving force of the redox replacement reactions between different redox pairs are attributed to the differences between the electrode potential values ($E$) calculated by the Nernst equation from 65 g/L Zn, 200 ppm Cu and 2 ppm Ag (temperature = 21 ± 0.5 °C, pH = 1.2):

$$Zn_{aq}^{2+} + 2e^- \rightleftharpoons Zn(s)\ E = -1.42\ V\ vs.Hg\Big/Hg_2SO_4 \quad (5)$$

$$Cu_{aq}^{2+} + 2e^- \rightleftharpoons Cu(s)\ E = -0.39\ V\ vs.Hg\Big/Hg_2SO_4 \quad (6)$$

$$Ag_{aq}^{+} + e^- \rightleftharpoons Ag(s)\ E = -0.13\ V\ vs.Hg\Big/Hg_2SO_4 \quad (7)$$

Nevertheless, under actual experimental conditions, the equilibrium potentials of the redox pairs will exhibit a shift from the calculated potentials [45]. In order to observe the actual equilibrium potentials where the redox reactions occur under experimental conditions, cyclic voltammetry (C*V*) measurements were performed using a glassy carbon (GC) electrode in a solution containing 2 ppm Ag, 200 ppm Cu, 65 g/L Zn and 10 g/L $H_2SO_4$. Fig. 1a shows the CV curve obtained within the potential range of −1.6 to +0.5 V (vs. Hg/$Hg_2SO_4$). As can be seen, the dramatic increase of negative current from ca. -1.45 V (vs. Hg/$Hg_2SO_4$) during the cathodic scan can be associated with the Zn deposition and the potential (−1.45 V) where this initiate is known as the nucleation potential. Typically, a notable nucleation overpotential (NOP, the potential difference between the nucleation potential and the crossover potential point—denoted as 'c' in Fig. 1a) can be observed in pure zinc solutions without impurities [46,47]. However, the NOP in Fig. 1a is negligible due to the marked depolarization effects of $Cu^{2+}$ and $Ag^{+}$ ions and similar phenomena have been previously reported [39]. On the other hand, the hydrogen evolution reaction is also inevitable when Zn reduction occurs as the potential is significantly lower and the potential of the redox pair $H^{+}/H_2$ (ca. -0.72 *V* vs. Hg/$Hg_2SO_4$). During the reverse scan, two distinct anodic peaks ($a_1$ and $a_2$) were obtained. Peak $a_1$ starting from −1.45 V relates to zinc dissolution while the other peak ($a_2$) is associated with Cu oxidation. The cathodic current density corresponding to Cu deposition is significantly lower compared to Zn deposition, as the electrochemical reduction of $Cu^{2+}$ is limited by the minor Cu concentration (200 ppm). Another C*V* measurement between −1.0 to +0.5 V (vs. Hg/$Hg_2SO_4$) was conducted for further investigation as shown in Fig. 1b. In this case, the cathodic peak (d) corresponds to the reduction of $Cu^{2+}$, whereas the anodic peak ($b_1$) in the reverse scan correlates with Cu dissolution. Furthermore, the actual redox potential of the $Cu^{2+}$/Cu shifted to a more negative value of ca. −0.50 *V* (vs. Hg/$Hg_2SO_4$) compared to the calculated potential ($E$ = −0.39 V vs. Hg/$Hg_2SO_4$). The small anodic peaks at $b_2$ are attributed to Ag dissolution and the starting potential was also found to be shifted to a more negative value of ca. −0.15 V (vs. Hg/$Hg_2SO_4$) cf. the calculated potential ($E$ = −0.13 V vs. Hg/$Hg_2SO_4$), while the reduction peak for $Ag^{+}$/Ag is not visible due to the extremely low Ag concentration (2 ppm).

Based on the findings from the CV studies, EDRR experiments were conducted using either Zn or Cu as the sacrificial metal. Fig. 1c shows an example of the potential and current density as a function of time during EDRR using Zn as the sacrificial metal with data from the first 5 cycles (from a total of 200 cycles) displayed for the sake of clarity. During an ED step, a constant potential $E_1$ is applied and the current is recorded, while during a RR step, no external potential or current is applied, but rather the spontaneous change in the open circuit potential (OCP) is merely recorded: for clarification, examples of the ED portion (ED@$E_1$) and RR portion (RR@OCP) are denoted in the potential curves shown in Fig. 1c and d. As can be seen, in a single EDRR cycle, Zn was firstly deposited with a short potential pulse (ED step) at −1.55 *V* (vs. Hg/$Hg_2SO_4$, $E_1$) for 0.5 s ($t_1$). A sharp decrease in the current density was observed in the ED step probably due to either electrochemical double-layer charging or nucleation [37,48,49]. A redox replacement (RR) step commences immediately after the ED step by cutting off the external electric charge for 5 s (i.e. redox replacement time $t_2$), such that the working electrode is left at open circuit potential and the current density was 0 mA/cm$^2$. In the RR step, the deposited Zn is spontaneously replaced by the $Cu^{2+}$ or $Ag^{+}$ ions as the potentials of redox pairs $Ag^{+}$/Ag and $Cu^{2+}$/Cu are more positive than the redox pair $Zn^{2+}$/Zn. An example of potential-current density-time curve - first 5 cycles out of 200 cycles - using Cu as the sacrificial metal is displayed in Fig. 1d, where Cu is pulse deposited in the ED step ($E_1$ = −0.70 *V* (vs. Hg/$Hg_2SO_4$), $t_1$ = 0.5 s) and the RR step was maintained for 5 s. In this case, the redox reaction occurs between the deposited Cu and $Ag^{+}$ ions due to the potential difference between redox pairs $Ag^{+}$/Ag and $Cu^{2+}$/Cu. Similar to the case with Zn as the sacrificial metal, a sharp decrease in the current density was also observed in the ED step probably also due to either electrochemical double-layer charging or nucleation. Moreover,

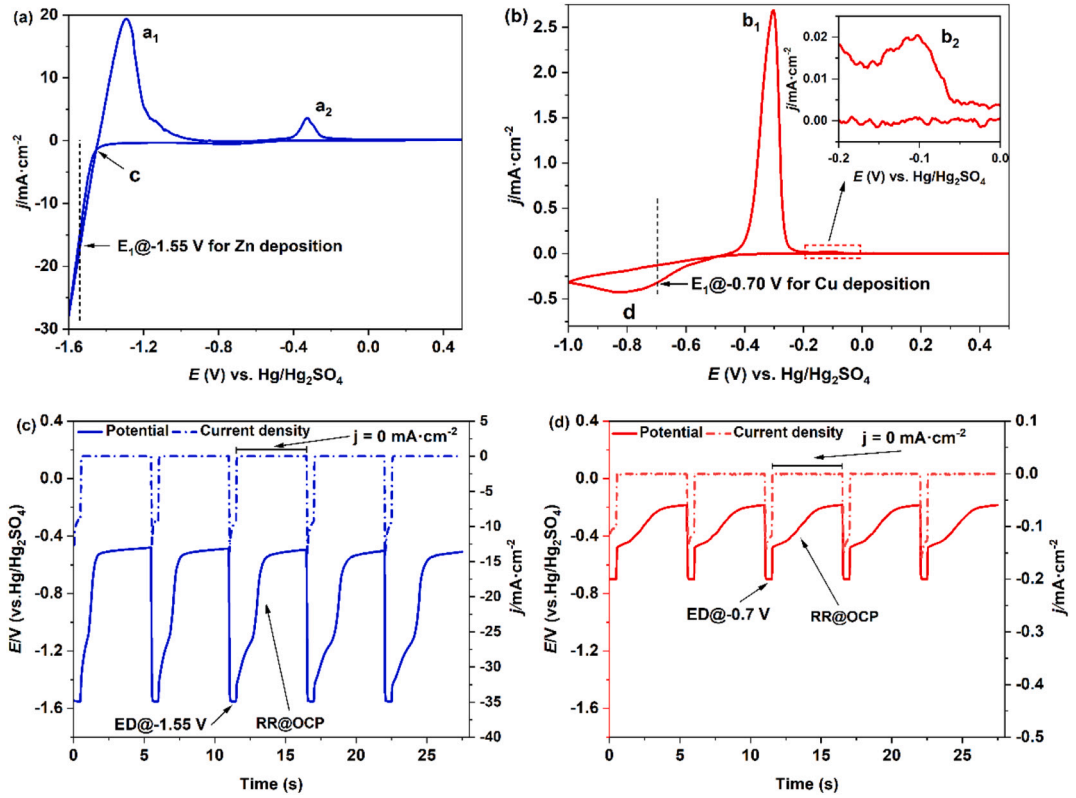


**Fig. 1.** Cyclic voltammetry of a GC electrode in a solution containing 2 ppm Ag, 200 ppm Cu, 65 g/L Zn and 10 g/L $H_2SO_4$ (20 m*V*/s) within the potential range of (a) -1.6 to +0.5 V (vs. $Hg/Hg_2SO_4$) and (b) -1.0 to +0.5 V (vs. $Hg/Hg_2SO_4$); (c) Potential−current density − time graphs (first 5 cycles) of the EDRR protocol using Zn as the sacrificial metal ($E_1 = -1.55$ V vs. $Hg/Hg_2SO_4$) and (d) Cu as the sacrificial metal ($E_1 = -0.70$ V vs. $Hg/Hg_2SO_4$). (N.B. Current scales are non-identical due to difference in Zn and Cu concentrations.)

in the ED steps, the current density using Cu as the sacrificial metal (Fig. 1d) was found to be significantly lower than when using Zn as the sacrificial metal (Fig. 1c) due to the mass-transfer limitations, as Cu is present at a significantly lower concentration (200 ppm) than Zn (65 g/L).

### 3.2. EDRR products using Zn as the sacrificial metal

Table 1 presents the detailed parameters for the preparation of 6 samples (S1-S6) using Zn as the sacrificial metal ($E_1 = -1.55$ *V* vs. $Hg/Hg_2SO_4$). The chemical compositions—obtained by EDS—of the deposits are also summarized in Table 1 while the related EDS spectra are presented in Fig. 2. As expected, the atom percentages of both Ag and Cu increased with replacement time as more Zn was replaced by $Ag^+$ and/or $Cu^{2+}$ ions. Meanwhile, the competing oxidation of Zn by $H^+$ ions ($H_2$ formation) can also decrease the Zn content, thereby further increasing Ag and Cu percentages. On the other hand, although the potential of the redox pair $Ag^+/Ag$ is more positive than that of $Cu^{2+}/Cu$, the Cu contents within all the samples are significantly higher than Ag. This finding is most likely due to the significant difference between the concentrations of $Cu^{2+}$ (200 ppm) and $Ag^+$ (2 ppm) ions. As the kinetics of redox replacement reactions are significantly affected by the concentration of the more-noble element [50], the markedly higher concentration of $Cu^{2+}$ ions compared to $Ag^+$ ions facilitates the reaction rate of redox replacement reaction between $Cu^{2+}$ ions and Zn, and consequently more Cu was deposited on the electrode. Moreover, in order to investigate the effects of increased EDRR cycles on the composition of Cu/Zn/Ag coatings, the EDS analysis of EDRR samples with 400 cycles has been conducted on two new samples prepared using the same $E_1$, $t_1$ and $t_2$ as sample S1 and S2. The results (Fig. S2) show that the composition of the deposits remained relatively stable when the EDRR cycles increased to 400.

**Table 1**
Parameters of EDRR experiments, the composition of Cu/Zn/Ag coatings by EDRR using Zn as the sacrificial metal ($E_1 = -1.55$ *V* vs. $Hg/Hg_2SO_4$), and the related current efficiencies.

| Sample ID | $t_1$ (s) | $t_2$ (s) | Composition (atom%) | | | $\eta$ (%) |
|---|---|---|---|---|---|---|
| | | | Cu | Zn | Ag | |
| S1 | 0.5 | 5 | 73.4 | 26.0 | 0.6 | 59.2 |
| S2 | 0.5 | 10 | 79.7 | 18.9 | 1.4 | 50.4 |
| S3 | 0.5 | 20 | 82.8 | 14.3 | 2.9 | 30.6 |
| S4 | 0.3 | 5 | 80.9 | 18.2 | 0.9 | 51.8 |
| S5 | 0.3 | 10 | 85.9 | 12.1 | 2.0 | 49.6 |
| S6 | 0.3 | 20 | 86.8 | 8.8 | 4.4 | 27.9 |

Fig. 3(a-c) shows that for the samples with a deposition time $t_1 = 0.5$ s (S1–S3) fine nucleation grains were obtained with a short replacement time $t_2 = 5$ s (S1), while with $t_2 = 10$ s (S2), the microstructure transformed into fine particles with a clear space between the different particles and a further increase in $t_2$ 20 s (S3) resulted in a rough surface with irregular projections. For the samples with a shorter deposition time $t_1 = 0.3$ s (S4 – S6), fine particles were obtained with $t_2 = 5$ s (Fig. 3d, S4) and a more compact/smoother microstructure was achieved with $t_2 = 10$ s (Fig. 3e, S5), while the surface with $t_2 = 20$ s has coarse shapes (Fig. 3f, S6). In general, the samples with $t_1 = 0.3$ s (S4 – S6) have more compact/smoother structures and smaller grain sizes than those produced when $t_1 = 0.5$ s (S1 – S3). This observation can be attributed to the following reasons: (i) Longer deposition times consume higher levels of $Zn^{2+}$ in the ED step and consequently, more $Ag^+$ or $Cu^{2+}$ ions can replace in the RR step. This leads to severe mass-transfer limitations during both steps, which results in spiky surfaces that can act as nucleation sites for dendritic growth; (ii) a longer $t_1$ of 0.5 s allows the

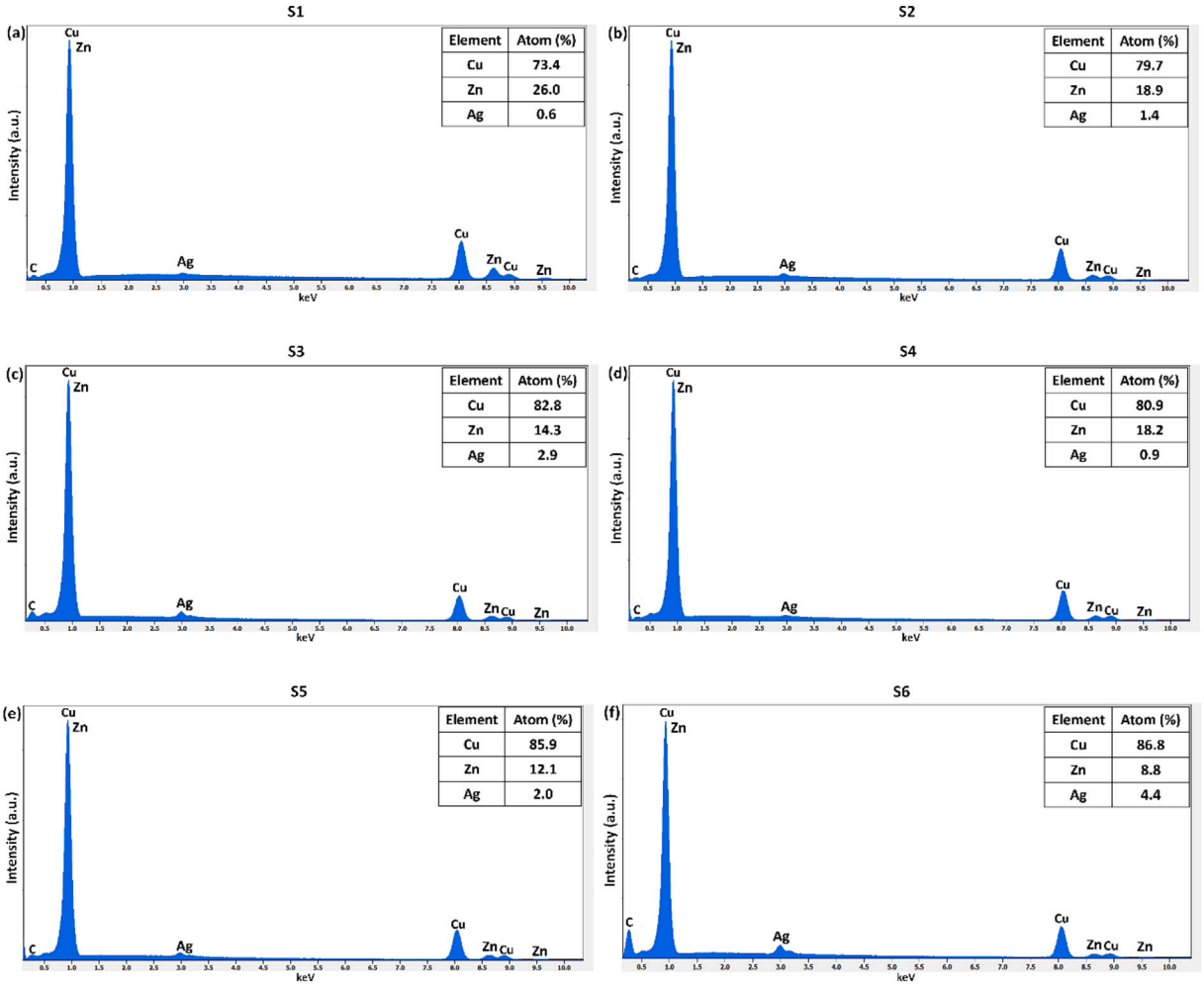


**Fig. 2.** (a)-(f) EDS spectra of Sample S1–S6.

nuclei formed in the initial stage to grow more extensively resulting in the larger grain sizes obtained [51]; (iii) more hydrogen gas accumulated in the samples with $t_1 = 0.5$ s, which can also lead to rougher and more unconnected surfaces [52].

The effect of parameters on the OCP values (recorded during the RR step in the absence of applied external potential or current) at the end of different EDRR cycles was collected and presented in Fig. 4a. Pure metals have different electrode potentials while alloys show a mixed potential - which is closely related to the electrode composition according to the mixed potential theory [53]. In general, the OCP values are in accordance with EDS results, i.e., higher OCP values were recorded with higher silver contents. On the other hand, the effect of mass-transfer limitation is clearly reflected in the variation of OCP values with the number of EDRR cycles within sample S1 ($t_1 = 0.5$ s, $t_2 = 5$ s). At the beginning of the experiment, $Cu^{2+}$ and $Ag^{+}$ in the vicinity of the electrode were sufficient and thus the OCP reached relatively high values due to the fast kinetics of the replacement reactions. Following the first tens of cycles, the OCP was observed to drop significantly to more negative values as $Cu^{2+}$ and $Ag^{+}$ ions were consumed and the redox replacement reactions were slowed down by mass-transfer limitations due to the short replacement time of 5 s. Similar results have also been reported when preparing Cu/Ag and Zn/Ag particles using the EDRR method from two components system [38,39] and Cu nanofilms by the SLRR method [54]. For samples S2-S5, the working electrodes showed more stable values with only slight variations due to improved mass-transfer conditions, as less Zn was deposited or the replacement times were longer for $Cu^{2+}$ and $Ag^{+}$ to migrate towards the electrode from the bulk solution. On the other hand, the higher OCP values with increased replacement times can be attributed to the formation of a surface passive layer [55]: a longer replacement time facilitates the establishment of a more stable passive layer on the surface due to the longer oxidation time and consequently, the observed OCP also shows more stable and positive values.

Fig. 4b shows the anodic linear stripping voltammograms (ALSV) together with the total stripping charge values of samples S1 – S6 in 0.1 M $H_2SO_4$. Potentiodynamic dissolution of pure Cu, Zn and Ag in $H_2SO_4$ solutions normally comprises unimodal peaks located at different potentials due to the distinct potentials of redox pairs $Ag^{+}$/Ag, $Cu^{2+}$/Cu and $Zn^{2+}$/Zn, however, in this case, only two stripping peaks ($a_1$, $a_2$) were detected on the EDRR samples in Fig. 4b. This can be explained by the fact that the dissolution of Zn and Cu appeared as only one peak ($a_1$), which is indicative of $Cu_xZn_{(1-x)}$ alloy phase formation [15,16]. Based on the potential of redox pair $Ag^{+}$/Ag and voltammetric studies of earlier studies, the stripping peak $a_2$ - starting from −0.1 V (vs. $Hg/Hg_2SO_4$) - can be associated with the dissolution of Ag [39]. The quantity of the dissolved species is proportional to the stripping charge density (area under the peak) of an anodic peak [15,16]. It can be seen that $a_2$ is not visible in S1 ($t_1 = 0.5$ s, $t_2 = 5$ s), as it is overlapped with $a_1$ due to the low Ag content (Table 1). When replacement time $t_2 = 10$ and 20 s, more Ag accumulates on the electrode and peak $a_2$ starts to appear on the ALSV curves of S2 and S3. A similar trend was also observed on the ALSV curves of S4 – S6 when $t_1 = 0.3$ s. The values of current efficiency ($\eta$), calculated based on the total stripping charge density, are also presented Table 1. Results show that the highest current efficiencies were achieved

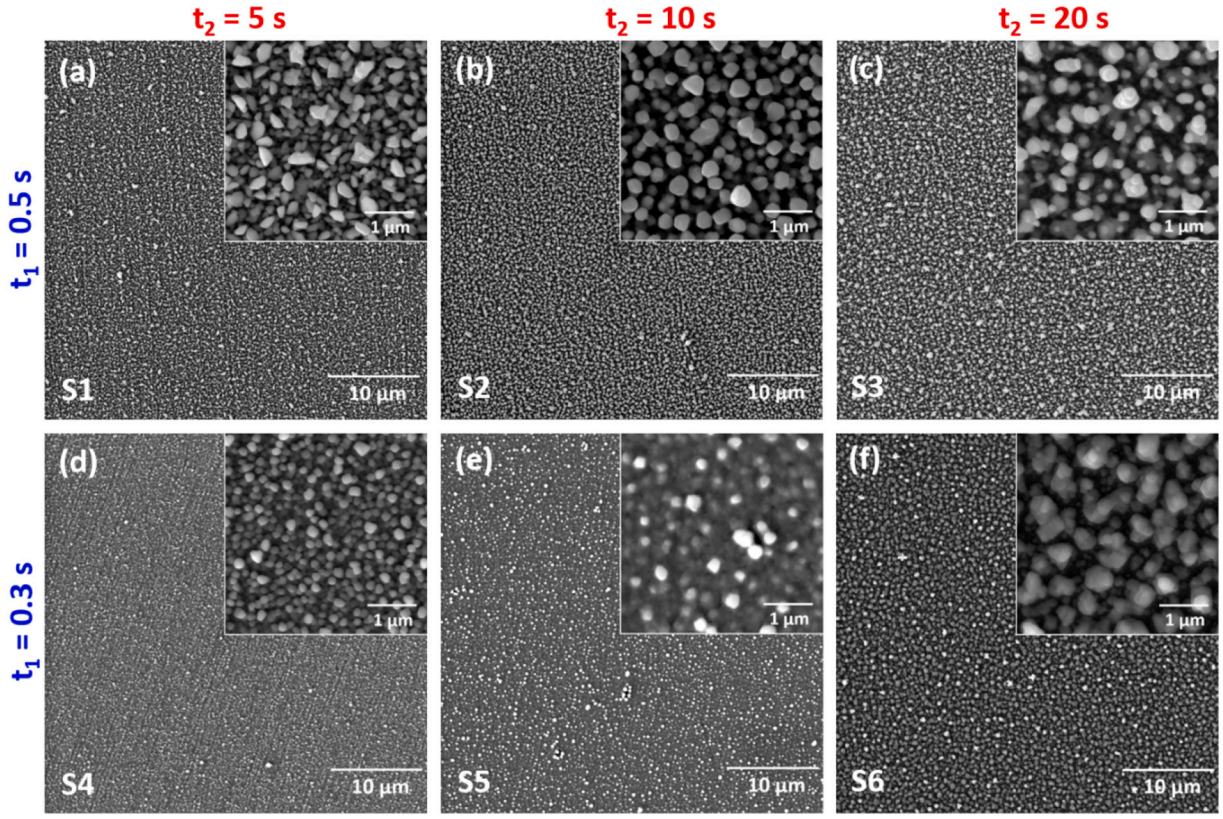


**Fig. 3.** (a)-(f) SEM images of GC electrodes after 200 EDRR cycles using Zn as the sacrificial metal ($E_1 = -1.55$ V vs. $Hg/Hg_2SO_4$) in a solution containing 65 g/L Zn, 200 ppm Cu, 2 ppm Ag and 10 g/L $H_2SO_4$ with varying $t_1$ and $t_2$.

for the samples with shortest replacement times (S1 and S4) and $\eta$ decreased with the increase of replacement time as indicated by a clear decrease in the total stripping charge density of $a_1$ and $a_2$ (Fig. 4b). The factors consuming the charge during EDRR can be attributed to the following side processes: (i) hydrogen evolution reaction (HER) during ED steps, (ii) competing oxidation of Zn by $H^+$ during RR steps and (iii) the non-faradic double layer established during every ED step in EDRR. When using the Zn as a sacrifical element these side reactions cannot be avoided as: (i) HER is inevitable due to the significantly lower Zn deposition potential when compared to the reduction potential of $H^+/H_2$; (ii) in addition to being replaced by $Cu^{2+}$ and $Ag^+$, the deposited Zn can also be oxidized by $H^+$ due to the potential difference between $H^+/H_2$ and $Zn^{2+}/Zn$ pairs, and (iii) the double-layer charging is a fundamental feature in electrochemistry that has also been observed for pulse deposition [56]. The EDRR current efficency values are, however, comparable with the previously reported values for traditional electrodeposition (ED) in literature. While the optimum current efficiency (59%) of this study was lower than ED from aqueous solutions with cyanide ($\eta = 80\%$) [11], EDTA (90%) [14] or glutamate (72%) [15], and from non-aqueous solutions like choline acetate electrolyte (74%) [20] and deep eutectic solvent (90%) [19], it was higher than the values reported in the presence of pyrophosphate (30%) [12], citrate (37%) [13] and sorbitol (54%) [16]. Also, it is important to note that in case of EDRR, no complexing agents were needed, hence lowering the overall environmental impact of the this method.

To identify the crystalline phases of the products, X-ray diffraction (XRD) analysis was performed and the results are displayed in Fig. 4c. As can be seen, samples with a short $t_2 = 5$ s (S1 and S4) primarily consist of a Cu-rich brass phase ($Cu_{0.75}Zn_{0.25}$), while the XRD peaks related to an independent Cu phase only begin to appear with prolonged replacement times (S2, S3, S5, S6) as more Zn is replaced by Ag and Cu. In contrast, peaks related to Ag with low intensity were only observed on the XRD patterns of samples with $t_2 = 20$ s (S1, S4), and were almost invisible for other samples due to the low Ag content.

Porous structures easily occur when using bulk galvanic displacement (i.e. cementation) due to the dissolution of the less-noble elements from the deposited matrix. To further investigate whether a similar phenomenon occurs during EDRR, the cross-section SEM image (Fig. 4d) for one of the Zn/Cu/Ag coating samples (S5) was undertaken, and the sample (S5) has a relatively compact structure compared to the porous structures using bulk galvanic displacement shown in the literature [57]. Such a difference is speculated to stem from the more "layer-to-layer" approach inherent to EDRR cycling where redox replacement occurs primarily on the upper-most layer in each cycle, in contrast to the selective dissolution of the matrix that occurs during bulk galvanic displacement.

### 3.3. EDRR products using Cu as the sacrificial metal

When using Cu as a sacrificial element (6 samples, Table 2 and the related EDS spectra are shown in Fig. 5), separated particles were obtained on the deposit (Fig. 6, S7–S12, $E_1 = -0.70$ *V* vs. $Hg/Hg_2SO_4$), different to coherent layer when using Zn (Fig. 3). This is associated with the considerable mass transfer limitation during the ED step due to the low concentration of sacrificial metal Cu (200 ppm). This correlates also with the cyclic voltammograms and EDRR profiles in Fig. 1. Since the potential of $Cu^{2+}/Cu$ is significantly higher than that of redox pair $Zn^{2+}/Zn$, the redox reaction only occurs between the deposited Cu and $Ag^+$ ions giving rise to the formation of Cu/Ag particles.

From Table 2 it can be determined that the particles formed at $t_2 = 5$ s (S7 and S10) mainly consist of Cu (≥65 atom%) due to the limited mass-transfer Ag ions. A clear transformation from Cu-rich particles to almost pure Ag particles (≥ 99 atom% Ag) is found with prolonged replacement times to 10 s, which allows more Ag to be incorporated

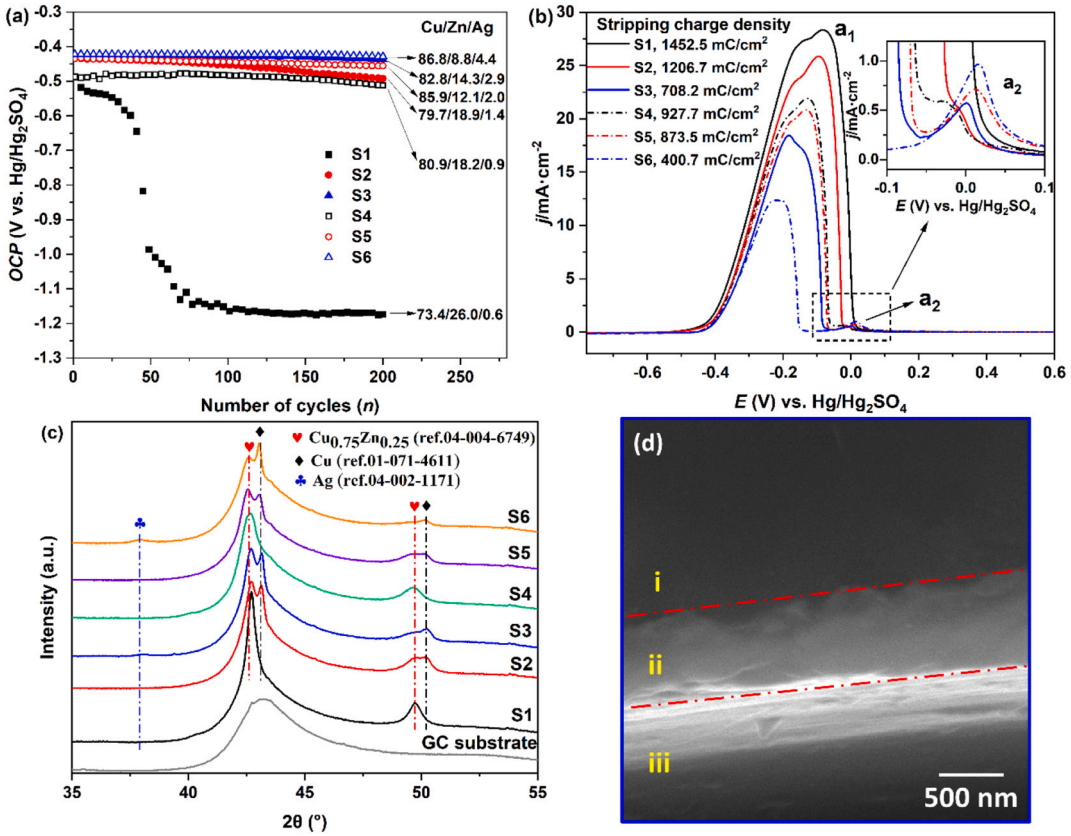


**Fig. 4.** (a) Open circuit potential (OCP) values at the ends of the EDRR cycles; (b) anodic linear stripping voltammograms (ALSV, 5 mV/s) and the total stripping charge density; (c) XRD patterns of EDRR samples; (d) cross-section image of Sample S5, region (i) corresponds to resin, while regions (ii) and (iii) are the cross-section and the bottom of the coating, respectively.

**Table 2**
Parameters of EDRR experiments, the composition of Cu/Ag particles by EDRR using Cu as the sacrificial metal ($E_1$ = −0.70 V vs. $Hg/Hg_2SO_4$), and the related current efficiencies.

| Sample ID | $t_1$ (s) | $t_2$ (s) | Composition (atom %) | | Particle size (nm) | $\eta$ (%) |
|---|---|---|---|---|---|---|
| | | | Cu | Ag | | |
| S7 | 0.5 | 2 | 84.8 | 15.2 | 115 ± 41 | 61.6 |
| S8 | 0.5 | 5 | 27.9 | 72.1 | 120 ± 34 | 25.4 |
| S9 | 0.5 | 10 | 0.6 | 99.4 | 170 ± 43 | 23.0 |
| S10 | 0.3 | 2 | 67.8 | 32.2 | 82 ± 13 | 50.6 |
| S11 | 0.3 | 5 | 0.9 | 99.1 | 116 ± 33 | 23.7 |
| S12 | 0.3 | 10 | 0.5 | 99.5 | 152 ± 40 | 21.6 |

within the particles. Nevertheless, lower Ag contents with $t_1 = 0.5$ s were evident compared to those with $t_1 = 0.3$ s (S10–S12). This can be attributed to the fact that due to the selected EDRR parameters there is less Cu on the surface to be replaced, therefore the available Ag is sufficient to allow full replacement and potentially also the smaller particle size obtained with $t_1 = 0.3$ s favors the reaction kinetics [58]. In addition, the particle size was found to increase with replacement time $t_2$, which may be a result of the stoichiometric ratio of Cu: Ag (1:2) of the replacement reaction as well as possible Ostwald ripening [38–40]. A similar phenomenon has been reported [38] in two metal systems where Cu is the dominant metal element (Cu 40 g/L, Zn 0 g/L) in the solution, however, the particle size of the Cu/Ag particles in the current study are clearly smaller (80–170 nm cf. 200–840 nm) due to the mass transfer limitation in the ED step.

Fig. 7a shows the compiled OCP values at the end of EDRR cycles when preparing S7 – S12 (i.e. using Cu as a sacrificial element). As can be seen, the OCP values correlate with the chemical compositions: the OCP of samples with bimetallic particles (S7, S8 and S10) reduced after the first few cycles to the mixed potential between Cu and Ag, whereas the other samples (S9, S11 and S12) have relatively stable OCP values (ca. -0.17 *V* vs. $Hg/Hg_2SO_4$) similar to pure Ag. Also, the higher OCP values with increased replacement times during the formation of Cu/Ag particles might be related to the surface passive layer similar to that discussed when Zn was deposited as the sacrificial metal [55]. The ALSV curves of samples S7 – S12 are presented in Fig. 7b and the results show that two distinct peaks were detected for the dissolution of Cu ($a_1$) and Ag ($a_2$) for samples S7, S8 and S10, which correlates with their bimetallic nature shown in Table 2. In contrast, only the Ag peak was observed for the other samples (S9, S11 and S12) and this correlates with the nearly pure Ag composition. It is indeed worth noting that even though the Zn is the predominant species in the solution (65 g/L) it was not detected within these samples, which clearly demonstrates how optimization of EDRR parameters can enable excellent selectivity between metals deposition, and even tailoring the composition of the surface. Compared to the samples with $t_2 = 5$ s (S7 and S10), the clear increase in the peak area of $a_2$ with longer replacement times confirmed the occurrence of redox replacement between the deposited Cu and $Ag^+$ ions, while the decrease of the overall stripping charge density indicates the presence of galvanic corrosion [59]. Similar to the case with Zn as the sacrificial element, the highest current efficiency was also achieved with $t_1 = 0.5$ and $t_2 = 5$ s, resulting in optimum current efficiency of 62%. Considering the relatively positive deposition potential applied, it is reasonable to assume that there is no hydrogen evolution reaction (HER) during ED steps, but rather the rest of the charge is consumed by non-faradic double-layer charging as indicated by the sharp increase of current density at the beginning of each ER step and the galvanic corrosion that occurs between Cu and Ag (i.e. re-dissolution of Cu) [60].

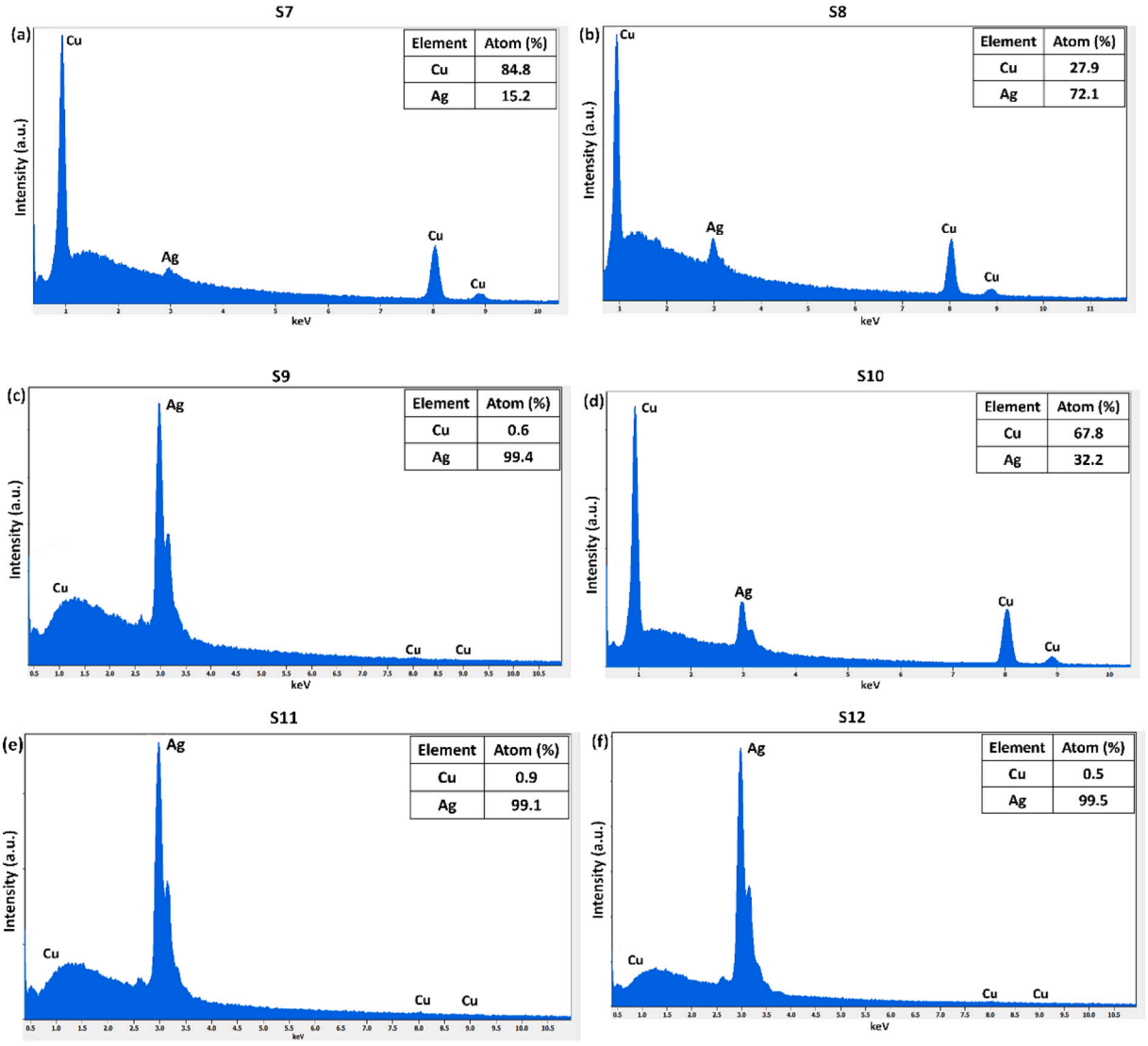


**Fig. 5.** (a)-(f) EDS spectra of Sample S7 – S12.

The XRD patterns in Fig. 7c highlight that in the bimetallic particles (S7, S8 and S10) Cu and Ag exist as independent crystalline phases, while for almost pure Ag particles (S9, S11 and S12) only Ag peaks are observed. Fig. 7d shows a high-resolution (magnification 30,000) SEM image of Sample S9 and it is seen the almost pure Ag particles (Ag atom % $\geq$ 99%) appear in a relatively compact structure due to the aforementioned "layer-by-layer" growth mode. This is in contrast to the porous/hollow nanoparticles previously prepared by galvanic replacement by Xia et al. [61] using prefabricated templates. Nonetheless, some of the particles by EDRR exhibit also a rougher surface as a result of the dissolution of Cu, both due to the redox replacement of the upper-most layers and corrosion that occurs in the presence of oxygen within the solution.

### 3.4. Targeted surface modification by EDRR based on sacrificial element selection

The results outlined above show that by careful selection of the parameters, EDRR in multimetal solutions permits the final composition and morphology of surfaces to be easily regulated by control of the sacrificial element. This allows surfaces with different functionalities to be formed from the same solution without any further system modifications such as the addition of complexing agents, etc. When Zn is utilized as a sacrificial element, more uniform coatings are formed, which have the potential to provide increased corrosion resistance. In contrast, the use of Cu leads to the formation of nanosized particles that can potentially be beneficial in optical applications based on surface plasmon resonance (SPR).

In order to examine the corrosion performance of the Cu/Zn/Ag coatings formed by EDRR, potentiodynamic polarization measurements were conducted for the relevant samples in a 3.5 wt% NaCl solution at room temperature (Fig. 8), whereas related corrosion potentials ($E_{corr}$) and corrosion current densities ($j_{corr}$) were evaluated by Tafel extrapolation (Table 3). Selected corrosion results from commercial brass samples and electrodeposited (ED) brass previously reported in the literature are also summarized in Table 3 for comparison.

In general, the corrosion potential of brass is closely related to the chemical composition as the $E_{corr}$ decreases with increased content of zinc [18] and such a trend also correlates with the brass by EDRR. For instance, the lowest $E_{corr}$ was observed on sample S1 which has the highest Zn percentage. Conversely, the sample with the lowest Zn content (S3) had a relatively higher $j_{corr}$ (e.g. poorer resistance) than the other samples due to the coarse morphology and the galvanic corrosion that takes place between the brass phase ($Cu_{0.75}Zn_{0.25}$) and the increased amount of independent Cu and Ag phases present [62]. When compared to brass produced by ED from sulfate/chloride solutions

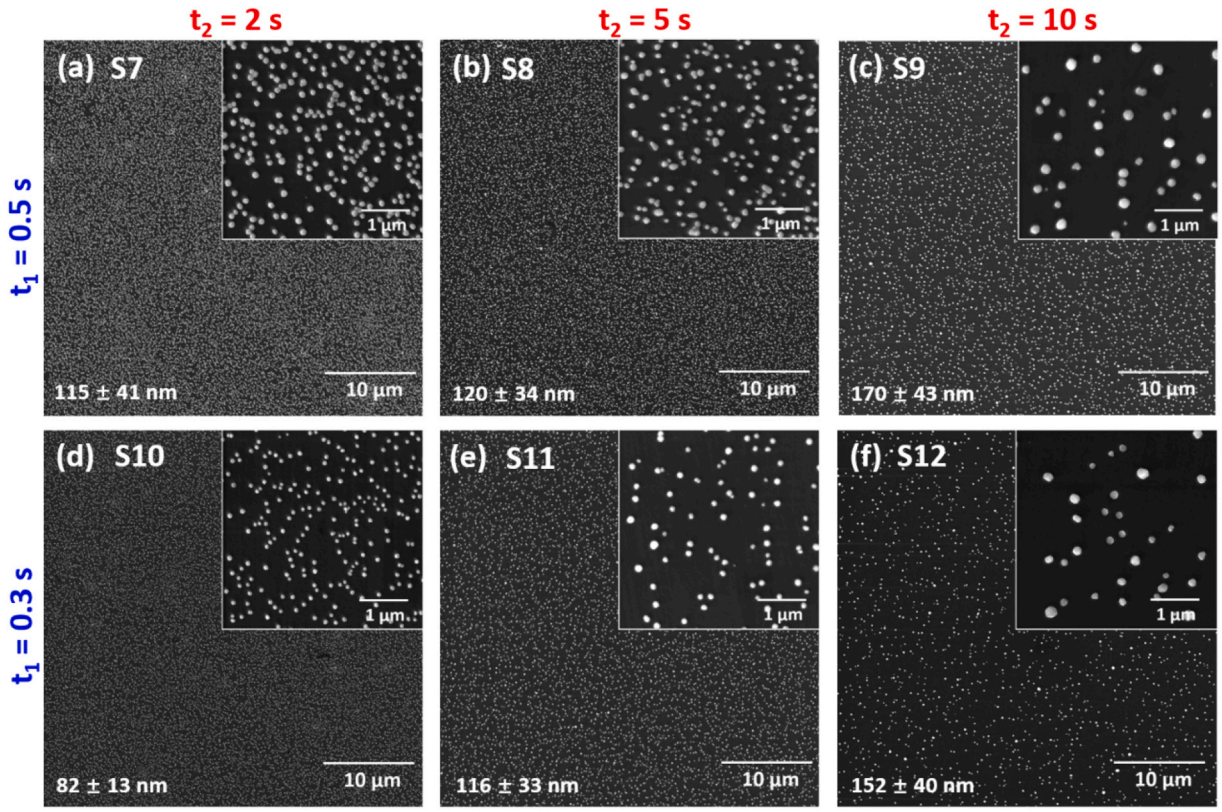


**Fig. 6.** (a)-(f) SEM images of GC electrodes after 200 EDRR cycles using Cu as the sacrificial metal ($E_1 = -0.70$ V vs. $Hg/Hg_2SO_4$) in a solution containing 65 g/L Zn, 200 ppm Cu, 2 ppm Ag and 10 g/L $H_2SO_4$ with varying $t_1$ and $t_2$.

containing trisodium citrate, commercial brass (Cu60-Zn40) and commercial brass (Cu65-Zn34 with trace impurities), the Cu/Zn-based deposits formed by EDRR exhibited an enhanced corrosion resistance (lower $j_{corr}$) [13,63,64], due to the presence of the Cu-rich phase, $Cu_{0.75}Zn_{0.25}$ (Table 3). Moreover, brass samples containing 43.4–83.8 Cu atom% obtained by ED from a ChCl/urea mixture also showed a similar corrosion resistance [18].

It is worth noting that potentiodynamic studies show only the susceptibility of a material to dissolve and are by no means a definitive proof of either corrosion performance or any related mechanisms. Consequently, the results outlined here for Cu/Zn/Ag coatings are indicative, therefore a more detailed investigation, using techniques like electrochemical impedance spectroscopy (EIS), would be needed to more fully elucidate the coating characteristics and related corrosion mechanisms—which is beyond the scope of this study. Nonetheless, these findings are promising in terms of corrosion prevention and when combined with the facts that EDRR requires no additional chemicals and can be performed at room temperature, there are significant advantages over traditional ED processes.

On the other hand, silver-based monometallic/bimetallic functional particles with unique optical properties that originate from the excitation of localized surface plasmon resonance (LSPR) can be used in different applications such as biological imaging and biosensing [65–68]. In order to explore the possible applications of the Cu/Ag and Ag particles produced by EDRR, the optical properties of samples S7 – S12 were characterized by UV/VIS spectroscopy (Fig. 9). From the results, it can be seen that clear absorption bands are present in the spectra of the EDRR samples due to LSPR, whereas no characteristic peak was detected on the blank GC substrate due to the characteristic black surface. The UV/VIS spectra of sample S7 exhibit a single absorption band at ca. 570 nm, which can be associated with its high Cu content (84.8 atom%) as absorption peaks in the range of 500–600 nm have been reported for pure Cu nanoparticles synthesized by chemical reduction [69–71]. In contrast, two absorbance peaks (ca. 320 nm and 420 nm, respectively) can be observed in the UV/VIS spectra of samples S8 and S10 due to the increased Ag content and similar dual-peak SPR phenomena have been found for similar Cu/Ag nanoparticles produced by chemical reduction [69,71,72]. When compared to previous investigations, the distinct absorption peak wavenumbers of these surfaces reflect the different properties, like particle size and dielectric environment, due to the EDRR method. Samples S9, S11 and S12 show a single-peak absorbance band at approximately 320 nm, that correlates with their almost pure Ag chemical composition [68–71]. Overall, these findings clearly demonstrate the ability to control SPR behavior by the variation of the selected EDRR parameters, thereby offering the possibility to produce desirable surface characteristics for a broad range of technological applications like surface-enhanced Raman scattering (SERS) [71] and water treatment [72].

## 4. Conclusions

This paper demonstrates the creation of multiple functional material surfaces directly from a Zn-based process solution (65 g/L Zn) containing minor concentrations of Cu (200 ppm) and Ag (2 ppm) using a one-cell electrodeposition-redox replacement approach. The EDRR method consists of repetitive steps of pulse-deposition of a less-noble sacrificial metal (ED) and the redox replacement (RR) by more noble metal ions. Coherent Cu/Zn/Ag coatings (Sample S1 – S6) controllable properties like chemical composition, surface morphology, crystalline phases could be obtained when Zn was selected as the sacrificial metal with 200 cycles of EDRR, whereas separate Cu/Ag particles (Sample S7 – S12) with tunable chemical composition, crystalline phases, and particle size (82–170 nm) were deposited from the same solution with an identical number of cycles when using Cu as the sacrificial metal. The whole process can be operated at room temperature without any complexing agents. In the case of Zn as the sacrificial metal, by controlling the

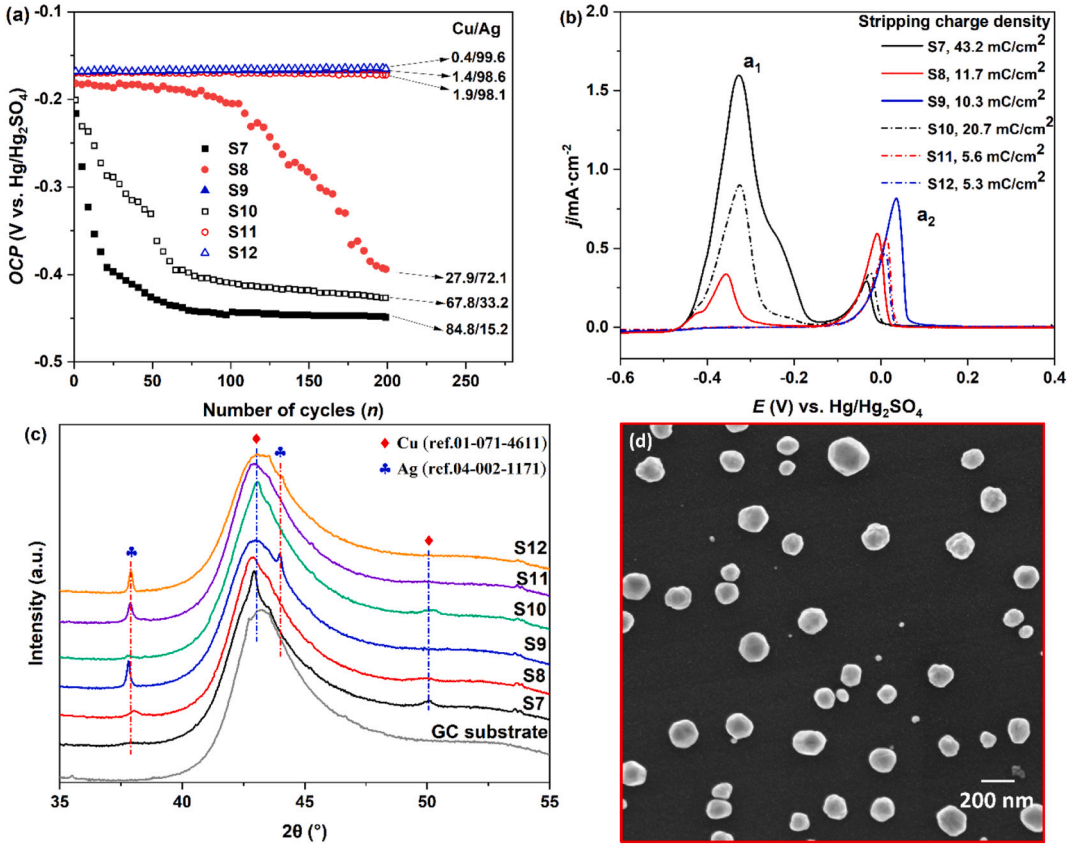


**Fig. 7.** (a) Open circuit potential (OCP) values at the end of the EDRR cycles; (b) anodic linear stripping voltammograms (ALSV, 5 mV/s) and the total stripping charge density; (c) XRD patterns of EDRR samples; (d) high-resolution SEM image of Sample S9.

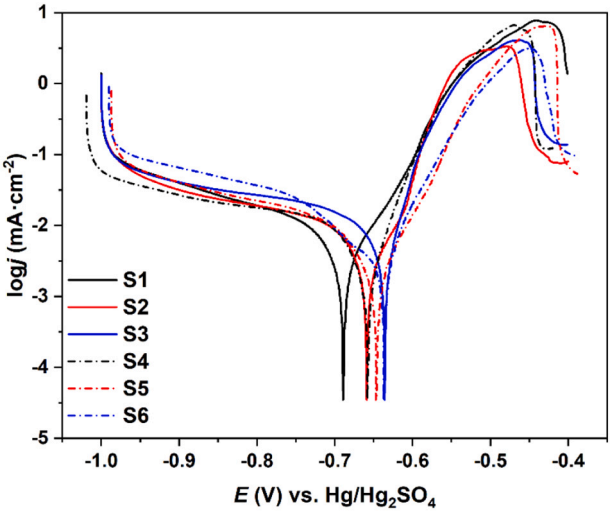


**Fig. 8.** Potentiodynamic polarization curves in a 3.5 wt% NaCl solution of the Cu/Zn/Ag coatings by EDRR using Zn as the sacrificial metal (S1 – S6, $E_1$ = −1.55 V vs. $Hg/Hg_2SO_4$).

operating parameters like deposition time and redox replacement time, the Cu/Zn/Ag coatings can be tailored to a range of corrosion potential ($E_{corr}$) from −683 to −634 mV vs. $Hg/Hg_2SO_4$ and related corrosion current density ($j_{corr}$) from 1.6 to 4.1 μA/cm$^2$. Alternatively, when Cu is utilized as the sacrificial metal, the Cu/Ag particles formed exhibited tunable surface plasmonic resonance (SPR) through the variation of operating parameters. The optimum current efficiencies were 59% for the formation of Cu/Zn/Ag coating and 62% for Cu/Ag particles, as

**Table 3**
Corrosion characteristics of Cu/Zn/Ag coatings by EDRR using Zn as the sacrificial metal ($E_1$ = −1.55 V vs. $Hg/Hg_2SO_4$) summarized from potentiodynamic polarization tests in 3.5 wt% NaCl solution.

| Sample ID | $E_{corr}$ (mV vs. $Hg/Hg_2SO_4$) | $J_{corr}$ (μA/cm$^2$) |
|---|---|---|
| S1 | −683 | 2.6 |
| S2 | −654 | 2.2 |
| S3 | −634 | 4.1 |
| S4 | −655 | 2.1 |
| S5 | −647 | 1.6 |
| S6 | −639 | 2.6 |
| Brass by ED from ChCl/urea mixture [18] | −1270 to −831 | 1.9–12.2 |
| Brass ED from sulfate/chloride solutions containing trisodium citrate [13] | −1003 to −903 | 19.0–42.0 |
| Commercial brass (Cu60-Zn40) [63] | −644 | 10.7 |
| Commercial brass (Cu65-Zn34 with trace impurities) [64] | −721 | 8.7 |

some of the current is consumed by side processes like double-layer charging, $H_2$ evolution and competing oxidation (corrosion) by $H^+$ ion. Overall, these results establish EDRR as a promising approach to exploit currently underutilized hydrometallurgical process solutions as a versatile solution for the manufacture of high value-added functional materials.

## CRediT authorship contribution statement

Zulin Wang: Conceptualization, Methodology, Investigation, Formal analysis, Writing – original draft.

Kirsi Yliniemi: Conceptualization, Methodology, Writing – review & editing, Supervision.

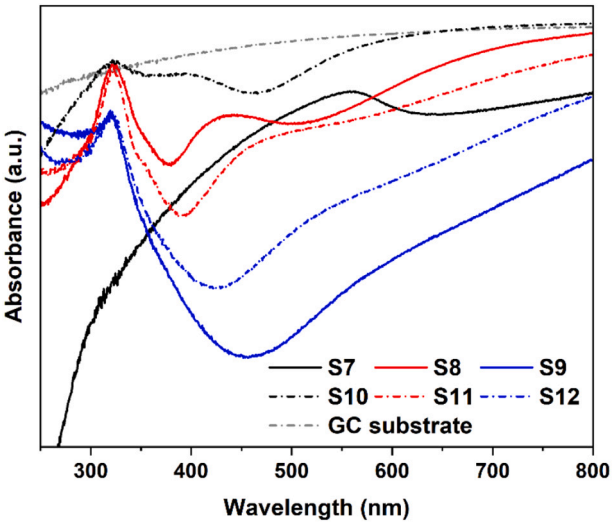


**Fig. 9.** UV/VIS spectra of the Cu/Ag particles by EDRR using Cu as the sacrificial metal (S7 – S12, $E_1 = -0.70$ V vs. $Hg/Hg_2SO_4$).

Benjamin P. Wilson: Conceptualization, Methodology, Writing – review & editing.

Mari Lundström: Conceptualization, Methodology, Supervision, Writing – review & editing, Funding acquisition, Resources, Project administration.

## Data availability statement

The data related this study are openly available in Zenodo at https://doi.org/10.5281/zenodo.5815216.

## Declaration of competing interest

The authors declare that they have no known competing financial interests or personal relationships that could have appeared to influence the work reported in this paper.

## Acknowledgment

Academy of Finland project (GoldTail (319691) BW) and EARMetal (339979, ML, KY) are greatly acknowledged for funding this research. The RawMatTERS Finland Infrastructure (RAMI) funded by Academy of Finland and based at Aalto University is also acknowledged. Moreover, the financial support from Chinese Scholarship Council (Grant No. 201706370244) and Finnish Foundation for Technology Promotion (grant No. 8188) is also appreciated by ZW.

## Appendix A. Supplementary data

Supplementary data to this article can be found online at https://doi.org/10.1016/j.surfcoat.2022.128531.

## References

[1] A. Tiwari, L. Uzun, Advanced Functional Materials, John Wiley & Sons, 2015.
[2] A. Brenner, Electrodeposition of Alloys: Principles and Practice, Elsevier, 2013.
[3] A. Varzi, L. Mattarozzi, S. Cattarin, P. Guerriero, S. Passerini, 3D porous Cu–Zn alloys as alternative anode materials for li-ion batteries with superior low T performance, Adv. Energy Mater. 8 (2018), 1701706, https://doi.org/10.1002/aenm.201701706.
[4] S.K. Bhogaraju, H.R. Kotadia, F. Conti, A. Mauser, T. Rubenbauer, R. Bruetting, M. Schneider-Ramelow, G. Elger, Die-attach bonding with etched micro Brass metal pigment flakes for high-power electronics packaging, ACS Appl. Electron. Mater. 3 (2021) 4587–4603, https://doi.org/10.1021/acsaelm.1c00721.
[5] H. Hu, Y. Tang, Q. Hu, P. Wan, L. Dai, X.J. Yang, In-situ grown nanoporous zn-cu catalysts on brass foils for enhanced electrochemical reduction of carbon dioxide, Appl. Surf. Sci. 445 (2018) 281–286, https://doi.org/10.1016/j.apsusc.2018.03.146.
[6] Y. Li, Y. Wu, B.S. Ong, Facile synthesis of silver nanoparticles useful for fabrication of high-conductivity elements for printed electronics, J. Am. Chem. Soc. 127 (2005) 3266–3267, https://doi.org/10.1021/ja043425k.
[7] Z. Xiu, Q. Zhang, H.L. Puppala, V.L. Colvin, P.J.J. Alvarez, Negligible particle-specific antibacterial activity of silver nanoparticles, Nano Lett. 12 (2012) 4271–4275, https://doi.org/10.1021/nl301934w.
[8] R. Xu, D. Wang, J. Zhang, Y. Li, Shape-dependent catalytic activity of silver nanoparticles for the oxidation of styrene, Chem. Asian J. 1 (2006) 888–893, https://doi.org/10.1002/asia.200600260.
[9] D.D. Evanoff Jr., G. Chumanov, Synthesis and optical properties of silver nanoparticles and arrays, ChemPhysChem 6 (2005) 1221–1231, https://doi.org/10.1002/cphc.200500113.
[10] K.J. Major, C. De, S.O. Obare, Recent advances in the synthesis of plasmonic bimetallic nanoparticles, Plasmonics 4 (2009) 61–78, https://doi.org/10.1007/s11468-008-9077-8.
[11] Y. Fujiwara, H. Enomoto, Electrodeposition of β′-Brass from cyanide baths with accumulative underpotential deposition of zn, J. Electrochem. Soc. 147 (2000) 1840, https://doi.org/10.1149/1.1393444.
[12] K. Johannsen, D. Page, S. Roy, A systematic investigation of current efficiency during brass deposition from a pyrophosphate electrolyte using RDE, RCE, and QCM, Electrochim. Acta 45 (2000) 3691–3702, https://doi.org/10.1016/S0013-4686(00)00461-8.
[13] C. Oulmas, S. Mameri, D. Boughrara, A. Kadri, J. Delhalle, Z. Mekhalif, B. Benfedda, Comparative study of Cu–Zn coatings electrodeposited from sulphate and chloride baths, Heliyon 5 (2019), e02058, https://doi.org/10.1016/j.heliyon.2019.e02058.
[14] M.R.H. de Almeida, E.P. Barbano, M.G. Zacarin, M.M. de Brito, P.C. Tulio, I. A. Carlos, Electrodeposition of CuZn films from free-of-cyanide alkaline baths containing EDTA as complexing agent, Surf. Coat. Technol. 287 (2016) 103–112, https://doi.org/10.1016/j.surfcoat.2015.12.079.
[15] M.A.M. Ibrahim, R.S. Bakdash, Copper-rich Cu–Zn alloy coatings prepared by electrodeposition from glutamate complex electrolyte: morphology, structure, microhardness and electrochemical studies, Surf. Interfaces 18 (2020), 100404, https://doi.org/10.1016/j.surfin.2019.100404.
[16] M.R.H. de Almeida, E.P. Barbano, M.F. de Carvalho, P.C. Tulio, I.A. Carlos, Copper–zinc electrodeposition in alkaline-sorbitol medium: electrochemical studies and structural, morphological and chemical composition characterization, Appl. Surf. Sci. 333 (2015) 13–22, https://doi.org/10.1016/j.apsusc.2015.02.005.
[17] S.M. Rashwan, Electrodeposition of Zn–Cu coatings from alkaline sulphate bath containing glycine, Trans. IMF 85 (2007) 217–224, https://doi.org/10.1179/174591907X216440.
[18] X. Xie, X. Zou, X. Lu, Q. Xu, C. Lu, C. Chen, Z. Zhou, Electrodeposition behavior and characterization of copper–zinc alloy in deep eutectic solvent, J. Appl. Electrochem. 47 (2017) 679–689, https://doi.org/10.1007/s10800-017-1069-y.
[19] X. Xie, X. Zou, X. Lu, C. Lu, H. Cheng, Q. Xu, Z. Zhou, Electrodeposition of zn and Cu–Zn alloy from ZnO/CuO precursors in deep eutectic solvent, Appl. Surf. Sci. 385 (2016) 481–489, https://doi.org/10.1016/j.apsusc.2016.05.138.
[20] P. De Vreese, A. Skoczylas, E. Matthijs, J. Fransaer, K. Binnemans, Electrodeposition of copper–zinc alloys from an ionic liquid-like choline acetate electrolyte, Electrochim. Acta 108 (2013) 788–794, https://doi.org/10.1016/j.electacta.2013.06.140.
[21] Y. Xue, Y. Wang, Green electrochemical redox mediation for valuable metal extraction and recycling from industrial waste, Green Chem. 22 (2020) 6288–6309, https://doi.org/10.1039/D0GC02028A.
[22] M. Singh, T. Ohji, R. Asthana, Green and Sustainable Manufacturing of Advanced Material, Elsevier, 2015.
[23] H. Sverdrup, D. Koca, K.V. Ragnarsdottir, Investigating the sustainability of the global silver supply, reserves, stocks in society and market price using different approaches, Resour. Conserv. Recycl. 83 (2014) 121–140, https://doi.org/10.1016/j.resconrec.2013.12.008.
[24] O.V. Belousov, N.V. Belousova, A.I. Ryumin, R.V. Borisov, Behavior of platinum metal concentrates under autoclave conditions, Russ. J. Appl. Chem. 88 (2015) 31–34, https://doi.org/10.1134/S107042721501005X.
[25] W. Wang, R. Li, T. Yuan, X. Zhu, H. Li, W. Lin, L. Li, Effects of Ag+ in diaphragm electrolysis on oxygen evolution and corrosion behaviors of pb and PbAg anodes, Hydrometallurgy 192 (2020), 105254, https://doi.org/10.1016/j.hydromet.2020.105254.
[26] W.G. Davenport, M.J. King, M.E. Schlesinger, A.K. Biswas, Extractive Metallurgy of Copper, Elsevier, 2002.
[27] F. Crundwell, M. Moats, V. Ramachandran, T. Robinson, W.G. Davenport, Extractive Metallurgy of Nickel, Cobalt and Platinum Group Metals, Elsevier, 2011.
[28] B.R. Reddy, B. Raju, J.Y. Lee, H.K. Park, Process for the separation and recovery of palladium and platinum from spent automobile catalyst leach liquor using LIX 84I and alamine 336, J. Hazard. Mater. 180 (2010) 253–258, https://doi.org/10.1016/j.jhazmat.2010.04.022.
[29] J. Mulwanda, C. Dorfling, Recovery of dissolved platinum group metals from copper sulphate leach solutions by precipitation, Miner. Eng. 80 (2015) 50–56, https://doi.org/10.1016/j.mineng.2015.07.002.
[30] K. Yliniemi, Z. Wang, I. Korolev, P. Hannula, P. Halli, M. Lundström, Effect of impurities in precious metal recovery by electrodeposition-redox replacement method from industrial side-streams and process streams, ECS Trans. 85 (2018) 59, https://doi.org/10.1149/08504.0059ecst.
[31] I. Korolev, P. Altinkaya, M. Haapalainen, E. Kolehmainen, K. Yliniemi, M. Lundström, Electro-hydrometallurgical chloride process for selective gold

recovery from refractory telluride gold ores: a mini-pilot study, Chem. Eng. J. 429 (2022), 132283, https://doi.org/10.1016/j.cej.2021.132283.
[32] I. Korolev, P. Altınkaya, P. Halli, P.-M. Hannula, K. Yliniemi, M. Lundström, Electrochemical recovery of minor concentrations of gold from cyanide-free cupric chloride leaching solutions, J. Clean. Prod. 186 (2018) 840–850, https://doi.org/10.1016/j.jclepro.2018.03.177.
[33] P. Halli, B.P. Wilson, T. Hailemariam, P. Latostenmaa, K. Yliniemi, M. Lundström, Electrochemical recovery of tellurium from metallurgical industrial waste, J. Appl. Electrochem. 50 (2020) 1–14, https://doi.org/10.1007/s10800-019-01363-6.
[34] P. Halli, H. Elomaa, B.P. Wilson, K. Yliniemi, M. Lundström, Improved metal circular economy-selective recovery of minor ag concentrations from zn process solutions, ACS Sustain. Chem. Eng. 5 (2017) 10996–11004, https://doi.org/10.1021/acssuschemeng.7b02904.
[35] P. Altinkaya, Z. Wang, I. Korolev, J. Hamuyuni, M. Haapalainen, E. Kolehmainen, K. Yliniemi, M. Lundström, Leaching and recovery of gold from ore in cyanide-free glycine media, Miner. Eng. 158 (2020), 106610, https://doi.org/10.1016/j.mineng.2020.106610.
[36] I. Korolev, S. Spathariotis, K. Yliniemi, B.P. Wilson, A.P. Abbott, M. Lundström, Mechanism of selective gold extraction from multi-metal chloride solutions by electrodeposition-redox replacement, Green Chem. 22 (2020) 3615–3625, https://doi.org/10.1039/D0GC00985G.
[37] Z. Wang, P. Halli, P. Hannula, F. Liu, B.P. Wilson, K. Yliniemi, M. Lundström, Recovery of silver from dilute effluents via electrodeposition and redox replacement, J. Electrochem. Soc. 166 (2019) E266, https://doi.org/10.1149/2.0031910jes.
[38] P.-M. Hannula, S. Pletincx, D. Janas, K. Yliniemi, A. Hubin, M. Lundström, Controlling the deposition of silver and bimetallic silver/copper particles onto a carbon nanotube film by electrodeposition-redox replacement, Surf. Coat. Technol. 374 (2019) 305–316, https://doi.org/10.1016/j.surfcoat.2019.05.085.
[39] Z. Wang, P.-M. Hannula, S. De, B.P. Wilson, J. Vapaavuori, K. Yliniemi, M. Lundström, Controllable production of Ag/Zn and ag particles from hydrometallurgical zinc solutions, ACS Sustain. Chem. Eng. 9 (2021) 8186–8197, https://doi.org/10.1021/acssuschemeng.1c01789.
[40] K. Yliniemi, N.T. Nguyen, S. Mohajernia, N. Liu, B.P. Wilson, P. Schmuki, M. Lundström, A direct synthesis of platinum/nickel co-catalysts on titanium dioxide nanotube surface from hydrometallurgical-type process streams, J. Clean. Prod. 201 (2018) 39–48, https://doi.org/10.1016/j.jclepro.2018.08.022.
[41] I.M. Ahmed, Y.A. El-Nadi, J.A. Daoud, Cementation of copper from spent copper-pickle sulfate solution by zinc ash, Hydrometallurgy 110 (2011) 62–66, https://doi.org/10.1016/j.hydromet.2011.08.007.
[42] K. Laatikainen, M. Lahtinen, M. Laatikainen, E. Paatero, Copper removal by chelating adsorption in solution purification of hydrometallurgical zinc production, Hydrometallurgy 104 (2010) 14–19, https://doi.org/10.1016/j.hydromet.2010.04.005.
[43] G. Owusu, Selective extraction of copper from acidic zinc sulfate leach solution using LIX 622, Hydrometallurgy 51 (1999) 1–8, https://doi.org/10.1016/S0304-386X(98)00062-0.
[44] S. Agarwal, A.E. Ferreira, S.M.C. Santos, M.T.A. Reis, M.R.C. Ismael, M.J. N. Correia, J.M.R. Carvalho, Separation and recovery of copper from zinc leach liquor by solvent extraction using acorga M5640, Int. J. Miner. Process. 97 (2010) 85–91, https://doi.org/10.1016/j.minpro.2010.08.009.
[45] X. Xia, Y. Wang, A. Ruditskiy, Y. Xia, 25th anniversary article: galvanic replacement: a simple and versatile route to hollow nanostructures with tunable and well-controlled properties, Adv. Mater. 25 (2013) 6313–6333, https://doi.org/10.1002/adma.201302820.
[46] D. Majuste, E.L.C. Martins, A.D. Souza, M.J. Nicol, V.S.T. Ciminelli, Role of organic reagents and impurity in zinc electrowinning, Hydrometallurgy 152 (2015) 190–198, https://doi.org/10.1016/j.hydromet.2015.01.003.
[47] N. Sorour, W. Zhang, G. Gabra, E. Ghali, G. Houlachi, Electrochemical studies of ionic liquid additives during the zinc electrowinning process, Hydrometallurgy 157 (2015) 261–269, https://doi.org/10.1016/j.hydromet.2015.09.003.
[48] J.-W. Kim, J.-Y. Lee, S.-M. Park, Effects of organic additives on zinc electrodeposition at iron electrodes studied by EQCM and in situ STM, Langmuir 20 (2004) 459–466, https://doi.org/10.1021/la0347556.
[49] M. Sánchez Cruz, F. Alonso, J.M. Palacios, Nucleation and growth of zinc electrodeposits on a polycrystalline zinc electrode in the presence of chloride ions, J. Appl. Electrochem. 23 (1993) 364–370, https://doi.org/10.1007/BF00296693.
[50] A.-A. El Mel, M. Chettab, E. Gautron, A. Chauvin, B. Humbert, J.-Y. Mevellec, C. Delacote, D. Thiry, N. Stephant, J. Ding, K. Du, C.-H. Choi, P.-Y. Tessier, Galvanic replacement reaction: a route to highly ordered bimetallic nanotubes, J. Phys. Chem. C 120 (2016) 17652–17659, https://doi.org/10.1021/acs.jpcc.6b06393.
[51] S. Xu, Y. Zhu, D. Xiong, L. Wang, P. Yang, P.K. Chu, Zinc electrodeposition on polycrystalline copper: electrochemical study of early-stage growth mechanism, J. Phys. Chem. C 121 (2017) 3938–3946, https://doi.org/10.1021/acs.jpcc.6b12036.
[52] H. Park, J. Choi, H. Kim, E. Hwang, D.-H. Ha, S.H. Ahn, S.-K. Kim, AgIn dendrite catalysts for electrochemical reduction of CO2 to CO, Appl. Catal. B Environ. 219 (2017) 123–131, https://doi.org/10.1016/j.apcatb.2017.07.038.
[53] N. Perez, Mixed potential theory, in: Electrochem. Corros. Sci, Springer US, Boston, MA, 2004, pp. 155–166, https://doi.org/10.1007/1-4020-7860-9_5.
[54] C. Thambidurai, D.K. Gebregziabiher, X. Liang, Q. Zhang, V. Ivanova, P.-H. Haumesser, J.L. Stickney, E-ALD of cu nanofilms on Ru/Ta wafers using surface limited redox replacement, J. Electrochem. Soc. 157 (2010), D466, https://doi.org/10.1149/1.3454213.
[55] T.H. Muster, I.S. Cole, The protective nature of passivation films on zinc: surface charge, Corros. Sci. 46 (2004) 2319–2335, https://doi.org/10.1016/j.corsci.2004.01.002.
[56] J. Cl, N.Ibl Puippe, Influence of charge and discharge of electric double layer in pulse plating, J. Appl. Electrochem. 10 (1980) 775–784, https://doi.org/10.1007/BF00611281.
[57] L.T. Viyannalage, Y. Liu, N. Dimitrov, Processing of nanoporous ag layers by potential-controlled displacement (PCD) of cu, Langmuir 24 (2008) 8332–8337, https://doi.org/10.1021/la800569t.
[58] C.M. Cobley, Y. Xia, Engineering the properties of metal nanostructures via galvanic replacement reactions, Mater. Sci. Eng. R. Rep. 70 (2010) 44–62, https://doi.org/10.1016/j.mser.2010.06.002.
[59] R.W. Revie, Uhlig's Corrosion Handbook, John Wiley & Sons, 2011.
[60] A.M.S.E. Din, L. Wang, Galvanic corrosion of copper/silver contacts in electrical switches, Br. Corros. J. 28 (1993) 271–278, https://doi.org/10.1179/000705993799156226.
[61] X. Xia, Y. Wang, A. Ruditskiy, Y. Xia, 25th anniversary article: galvanic replacement: a simple and versatile route to hollow nanostructures with tunable and well-controlled properties, Adv. Mater. 25 (2013) 6313–6333, https://doi.org/10.1002/adma.201302820.
[62] N. North, The role of galvanic couples in the corrosion of shipwreck metals, Int. J. Naut. Archaeol. 13 (1984) 133–136, https://doi.org/10.1111/j.1095-9270.1984.tb01183.x.
[63] M. Damej, D. Chebabe, S. Abbout, H. Erramli, A. Oubair, N. Hajjaji, Corrosion inhibition of brass 60Cu–40Zn in 3% NaCl solution by 3-amino-1, 2, 4-triazole-5-thiol, Heliyon 6 (2020), e04026, https://doi.org/10.1016/j.heliyon.2020.e04026.
[64] R. Ravichandran, S. Nanjundan, N. Rajendran, Effect of benzotriazole derivatives on the corrosion of brass in NaCl solutions, Appl. Surf. Sci. 236 (2004) 241–250, https://doi.org/10.1016/j.apsusc.2004.04.025.
[65] M. Fan, M. Thompson, M.L. Andrade, A.G. Brolo, Silver nanoparticles on a plastic platform for localized surface plasmon resonance biosensing, Anal. Chem. 82 (2010) 6350–6352, https://doi.org/10.1021/ac101495m.
[66] G. Steiner, Surface plasmon resonance imaging, Anal. Bioanal. Chem. 379 (2004) 328–331, https://doi.org/10.1007/s00216-004-2636-8.
[67] M.I. Stockman, Nanoplasmonic sensing and detection, Science 348 (2015) 287–288, https://doi.org/10.1126/science.aaa6805.
[68] T. Ghodselahi, S. Arsalani, T. Neishaboorynejad, Synthesis and biosensor application of Ag@Au bimetallic nanoparticles based on localized surface plasmon resonance, Appl. Surf. Sci. 301 (2014) 230–234, https://doi.org/10.1016/j.apsusc.2014.02.050.
[69] N.M. Zain, A.G.F. Stapley, G. Shama, Green synthesis of silver and copper nanoparticles using ascorbic acid and chitosan for antimicrobial applications, Carbohydr. Polym. 112 (2014) 195–202, https://doi.org/10.1016/j.carbpol.2014.05.081.
[70] M.C. Dang, T.M.D. Dang, E. Fribourg-Blanc, Inkjet printing technology and conductive inks synthesis for microfabrication techniques, Adv. Nat. Sci. Nanosci. Nanotechnol. 4 (2013), 015009, https://doi.org/10.1088/2043-6262/4/1/015009.
[71] D. Zhang, X. Liu, Synthesis of polymer-stabilized monometallic cu and bimetallic Cu/Ag nanoparticles and their surface-enhanced raman scattering properties, J. Mol. Struct. 1035 (2013) 471–475, https://doi.org/10.1016/j.molstruc.2012.12.023.
[72] M. Ismail, M.I. Khan, S.B. Khan, M.A. Khan, K. Akhtar, A.M. Asiri, Green synthesis of plant supported CuAg and CuNi bimetallic nanoparticles in the reduction of nitrophenols and organic dyes for water treatment, J. Mol. Liq. 260 (2018) 78–91, https://doi.org/10.1016/j.molliq.2018.03.058.